PHOTONICS Research

Real-time noise-free inline self-interference incoherent digital holography with temporal geometric phase multiplexing

Kihong Choi,[1,†] Jae-Won Lee,[2,†] Jungyeop Shin,[2] Keehoon Hong,[1] Joongki Park,[1] and Hak-Rin Kim[2,3,*]

[1]Digital Holography Research Section, Electronics and Telecommunications Research Institute, Daejeon 34129, Republic of Korea
[2]School of Electronic and Electrical Engineering, Kyungpook National University, Daegu 41566, Republic of Korea
[3]School of Electronics Engineering, Kyungpook National University, Daegu 41566, Republic of Korea
[†]These authors contributed equally to this work.
*Corresponding author: rineey@knu.ac.kr

Received 23 September 2022; revised 9 February 2023; accepted 25 February 2023; posted 27 February 2023 (Doc. ID 476354); published 4 May 2023

In this paper, we propose a real-time incoherent digital holographic (IDH) recording system free from bias and twin-image noises. A motionless three-step polarization-encoded phase-shifter operating at 99 Hz is realized with two electrically controllable birefringence-mode liquid crystal cells operating in tandem with a geometric phase lens and polarizers. Based on the proposed optical configuration, a coaxial straight-line self-interference IDH recording system is devised. Notably, the elimination of bias and twin-image noise from three phase-shifted images is demonstrated as a proof of concept. Moreover, complex-valued holographic video acquisitions with a resolution greater than 20 megapixels are demonstrated, with an effective acquisition frequency of 33 Hz.

https://doi.org/10.1364/PRJ.476354

1. INTRODUCTION

Incoherent digital holography (IDH) is a technology that acquires holograms digitally under various lighting conditions beyond those enabled by a laser [1–3]. Therefore, the advantage of acquiring holographic 3D light information can be subsequently used in more diverse applications. For instance, to the best of our knowledge, a holographic acquisition of a microbiological sample using fluorescent labeling [4,5] or an outdoor scene under sunlight [6] has not been achieved with laser-based conventional holographic interferometers. In the meantime, the problem of bias and twin-image noise, which is a classical problem of holographic interferometers because of the nature of interference, must also be solved for noise-free IDH capture. Various solutions have been suggested to address this problem not only in the field of coherent holography but also in the IDH field.

Most of the techniques to remove bias and twin-image noise from interferograms are classified according to whether real-time recording is available. Several methods, such as the off-axis configuration method [7–9], iterative phase retrieval method [10,11], and learning-based methods [12–14], have been proposed to realize real-time recording while reducing the bias and twin-image noise. Notably, the phase-shifting technique accurately eliminates the bias and twin-image noise without sacrificing the bandwidth of the image sensor, requiring additional computation time for iteration, or estimating the probable solution using a neural network. However, stepwise recording of phase-shifted interferograms is required in this method, which inevitably reduces the temporal resolution of the system.

An intuitive method to induce a phase delay is to change the propagating path lengths of two interfering beams in an interferometer. For example, in a self-interference incoherent digital holography system, one of the mirrors in the Michelson or Mach–Zehnder interferometer can be mounted on a piezoelectric transducer and actuated in a stepwise manner to sequentially induce a phase delay between the self-interfering wavefronts [6,15]. Moreover, the phase delay can be controlled both by physical distance modification and by optical path length modulation when light passes through the birefringent material. Specifically, phase-only spatial light modulators (SLMs) or liquid crystal (LC) based variable waveplates are employed in Fresnel incoherent correlation holography (FINCH) [16,17]. Simple rotation of the polarizer or waveplate also induces a phase delay between the interfering wavefronts, which is referred to as geometric phase (GP) shifting [18–20]. Particularly, the optical configuration comprises an input polarizer and a GP lens, and the output polarizer is introduced

for incoherent holographic recording [21]. In this system, the relative rotation angle δ between the polarizers results in a phase shift of 2δ in the interferogram. The stepwise rotation of a quarter-wave plate employed in one of the arms of a Michelson interferometer induces the same effect [22].

To overcome the temporal resolution loss entailed by the phase-shifting method in holographic recording systems, modified FINCH systems with a randomly multiplexed bifocal diffractive lens [23], multiplexed checkerboard phase gratings with two SLMs [24], spatially divided diffractive lenses [25], and diffractive phase gratings with a four-segmented linear polarizer [26], have been adopted for single-shot hologram capture. Furthermore, a spatial phase multiplexing technique, called the parallel phase-shifting method, has also been developed [27,28]. Specifically, a polarized image sensor, wherein four angled (90°, 45°, 135°, and 0°) wire-grid polarizers are fabricated on each pixel, is employed in this technique. Single-shot incoherent holography is realized in FINCH-based systems with a phase-only SLM [29], birefringent lens [30], or GP lens [31–33]. As reported based on several single-shot IDH systems, using a polarized image sensor promotes real-time hologram acquisition. However, four polarized sub-pixel values must be combined into a single superpixel value to generate a complex-valued hologram free from bias and twin-image noises. This process reduces the total number of pixels both in the horizontal and vertical directions of the reconstructed image by half. Additionally, the acquirable high-frequency information near the Nyquist frequency defined by the effective pixel size and the input wavelength of light is also decreased by half. In this context, studies to minimize the pixel size in polarized image sensors have been reported, but this is challenging while simultaneously optimizing the factors underlying overall polarimetric imaging quality, such as the polarization characteristics, quantum efficiency, and angle of incidence [34].

In this paper, we propose a real-time incoherent digital holographic recording system using a fast temporally polarization-encoded phase-shifting scheme. Particularly, the fast-switching polarization controller unit comprises two bi-stacked retardation-controllable LC cells, a geometric phase lens, and polarizers. As a proof of concept, we demonstrated real-time incoherent hologram recording with a resolution of up to 20 megapixels. The frame rate of the recorded video sample is 33 Hz. This is the result of three-step sequentially phase-shifted interferograms recorded at 99 Hz using the nonpolarized image sensor. The temporal resolution of the proposed method is threefold lower than that of the parallel phase-shifting method; nevertheless, an effective recording speed of more than 30 Hz is achieved, thereby providing a reasonable temporal resolution for real-time video recording. In addition, because all components are arranged coaxially as in the optical system of a general camera, the system configuration is simple, and no mechanical movement is required for the phase shift. Consequently, stable high-speed hologram acquisition is possible. In the following section, the principle of operation of the incoherent recording system, which employs the geometric phase effect and the phase-shifting method proposed here, is described. Subsequently, a proof-of-concept experimental setup is described, and the demonstration of a real-time hologram acquisition is presented.

2. OPERATION PRINCIPLE

A. Incoherent Hologram Acquisition with Geometric Phase Shifting

A schematic of the proposed method is presented in Fig. 1. The GP lens serves as a convex lens $(+f)$ to the right-handed circularly polarized (CP) light input and as a concave lens $(-f)$ to the left-handed CP light. Linear polarization can be regarded as the vector sum of both right and left-handed CP lights; therefore, two states of wavefronts are generated after the light passes through the GP lens with different radii of curvature. The GP lens comprises spatially aligned birefringent molecules or dielectric nanoscale structures, each of which serves as a unit half-wave plate. LCs are generally used to fabricate GP lenses because of their versatile alignment capability [35,36]. The alignment angle Ψ of the unit structure can be determined based on its spatial positions x and y, the central wavelength λ, and intended focal length f, as

$$\Psi(x,y) = \frac{2\pi}{\lambda}\left(\sqrt{x^2+y^2+f^2} - f\right). \tag{1}$$

The wave propagation through the system can be described as beginning from the spherical wave reflected by the object or the self-illuminated by the object itself. Because such light is likely to be nonpolarized, a linear polarizer is used to define

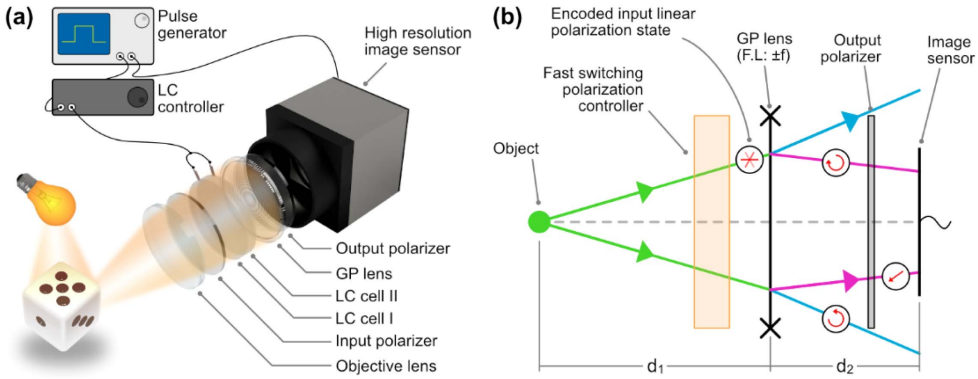

Fig. 1. (a) Schematic of the proposed method. (b) Diagram of the simplified system with optical parameters and polarization states of each ray. F.L., focal length.

the initial polarization state before passing through the GP lens. The field immediately before the GP lens corresponds to the spherical wave diverged from the point light source with the wavelength λ, located at a distance d_1 from the GP lens. Then, the divided fields immediately after the GP lens with focal lengths of $\pm f$ can be described as $\exp[-j\pi\lambda^{-1}(1/d_1 \pm 1/f)\cdot(x^2+y^2)]$.

After further propagation toward the image sensor, corresponding to a distance d_2, the field is still assumed to be a spherical wave. The recorded intensity is the result of self-interference between the two orthogonal circularly polarized wavefronts. Therefore, a second polarizer is required to simultaneously define the polarization states of two wavefronts. The final field u_s at the image sensor plane is expressed as

$$u_s = \exp\left\{\frac{j\pi}{\lambda[d_1 f/(f-d_1)+d_2]}(x^2+y^2)\right\} + \exp\left\{\frac{j\pi}{\lambda[d_1 f/(f+d_1)+d_2]}(x^2+y^2)\right\}. \quad (2)$$

We denote the first term in Eq. (2) as $Q(+f)$ and the second term as $Q(-f)$. The amplitude coefficients of the first and second terms are c_1 and c_2, respectively. Then, the result of interference is

$$\begin{aligned} I(x,y;\delta) &= |c_1 Q(+f)e^{j\delta} + c_2 Q(-f)e^{-j\delta}|^2 \\ &= c_1^2 + c_2^2 + c_1 c_2 \exp\left[\frac{j\pi}{\lambda z_r}(x^2+y^2) + j\delta\right] \\ &\quad + c_1 c_2 \exp\left[-\frac{j\pi}{\lambda z_r}(x^2+y^2) - j\delta\right], \end{aligned} \quad (3)$$

where δ is related to the phase-shifting value discussed later. Here, z_r refers to the reconstruction distance of the hologram, which can be calculated as $[d_2^2/f - f(1+d_2/d_1)^2]/2$.

Our goal is to remove the first two terms and the last term from Eq. (3). To this end, we devise a high-speed phase-shifting technique comprising an optical circuit equivalent to an input polarizer, a half-wave plate, and an output polarizer. We refer to this scheme as the P-GP-P structure [20,21]. More specifically, the input polarization state is defined as a sequential combination of voltage values applied to two LC cells. Although the results of the mechanical rotation of the input polarizer and the driving of two LC cells are identical, the LC cell enables a high-speed polarization state change while maintaining the stability of the recording system. The details of the fast switching polarization control scheme for real-time incoherent hologram recording are described in the following subsection. The amount of phase shift of the interferogram $I(x,y;\delta)$ according to the input linear polarization angle can be calculated using the Jones calculus method. Starting from an arbitrary angle δ of the input polarization state $[\cos\delta; \sin\delta]$, the output Jones vector after the horizontally aligned output polarizer is calculated as

$$\begin{pmatrix} 1 & 0 \\ 0 & 0 \end{pmatrix} R(-\Psi) \begin{pmatrix} -j & 0 \\ 0 & j \end{pmatrix} R(\Psi) \begin{pmatrix} \cos\delta \\ \sin\delta \end{pmatrix} = -j \begin{pmatrix} \cos(2\Psi-\delta) \\ 0 \end{pmatrix}, \quad (4)$$

where $R(\theta)$ is the rotation matrix (i.e., $[\cos\theta, \sin\theta; -\sin\theta, \cos\theta]$), and Ψ is the angle of the spatially varying slow-axis of the GP lens as a half-wave plate, which can be determined using Eq. (1). The transmittance of the output Jones vector is then calculated as $\frac{1}{2} + \mathrm{Re}\{\exp[i(4\Psi - 2\delta)]\}/2$. The result reveals that a phase-shift of 2δ is induced by the rotation of the input polarizer by an angle δ. Therefore, to apply the three-step phase-shifting method with the described method, the required δ values are 0°, 60°, and 120°. Note that the angle of the output polarizer does not need to be horizontal, and it can be an arbitrary angle. This is because only the phase difference between two succeeding interferograms is considered. The complex hologram U_{init}, free from bias and twin-image noise, can be determined as

$$U_{\mathrm{init}} = I_1(e^{j\delta_3} - e^{j\delta_2}) + I_2(e^{j\delta_1} - e^{j\delta_3}) + I_3(e^{j\delta_2} - e^{j\delta_1}), \quad (5)$$

where I_k is the kth phase-shifted interferogram, and the phase-shifting angles $[\delta_1, \delta_2, \delta_3]$ are $[0, 2\pi/3, 4\pi/3]$, respectively [37].

Here, the widely used angular spectrum method is used to retrieve the object scene from the hologram [38]. To retrieve a field U_z that has propagated by a distance of z_r from U_{init}, the spatial frequency transfer function $\mathcal{H}(k_x, k_y; z)$ with the frequency domain coordinates (k_x, k_y) is applied to the initial field, which can be described as

$$U_z(x,y;z_r) = \mathcal{F}^{-1}[\mathcal{F}\{U_{\mathrm{init}}(x,y)\} \times \mathcal{H}(k_x, k_y; z_r)]. \quad (6)$$

For wave number $k_0 = 2\pi/\lambda$, where λ is the central wavelength of the input light source, the transfer function $\mathcal{H}$ is expressed as

$$\mathcal{H}(k_x, k_y; z_r) = \exp\left[jk_0 z_r \sqrt{1 - \lambda^2(k_x^2 + k_y^2)}\right]. \quad (7)$$

The resultant image of the retrieved field is the intensity-valued data $|U_z|^2$, which is expressed as a 2D array of 8-bit unsigned integer values.

B. Fast-Switching Polarization Control for Temporally-Polarization-Encoded Phase-Shifting

As described in Eqs. (4) and (5), the multisteps of the phase-shifting scheme can be employed in the holographic image reconstruction step with the IDH system with the P-GP-P structure by modulating an incident polarization state with respect to a fixed analyzer angle condition, instead of using spatially patterned analyzer sets [31]. With this temporally polarization-encoded phase-shifting approach, the holographic image resolution can be effectively enhanced, but sequentially switched polarization states must be precisely controlled to avoid phase errors during image reconstruction. In addition, the switching time between the polarization states, required for multistep phase-shifting should be as short as possible to allow sufficient image acquisition time in the camera to suppress the image noise level.

Figure 2(a) shows the fast-switching polarization controller unit employed in the P-GP-P structure for time-sequential operation of the three-step phase-shifting. The three-steps of polarization modulation can be achieved by using bi-stacked retardation-controllable LC cells [LC cell I and LC cell II in Fig. 2(a)]. In bi-stacked LC cells, each LC cell has an electrically controllable birefringence mode, which is optically operated as an a-plate retarder and c-plate retarder in the field-off and field-on operation states, respectively [39]. In particular, the employed LC cells are designed to function as half-wave retarders

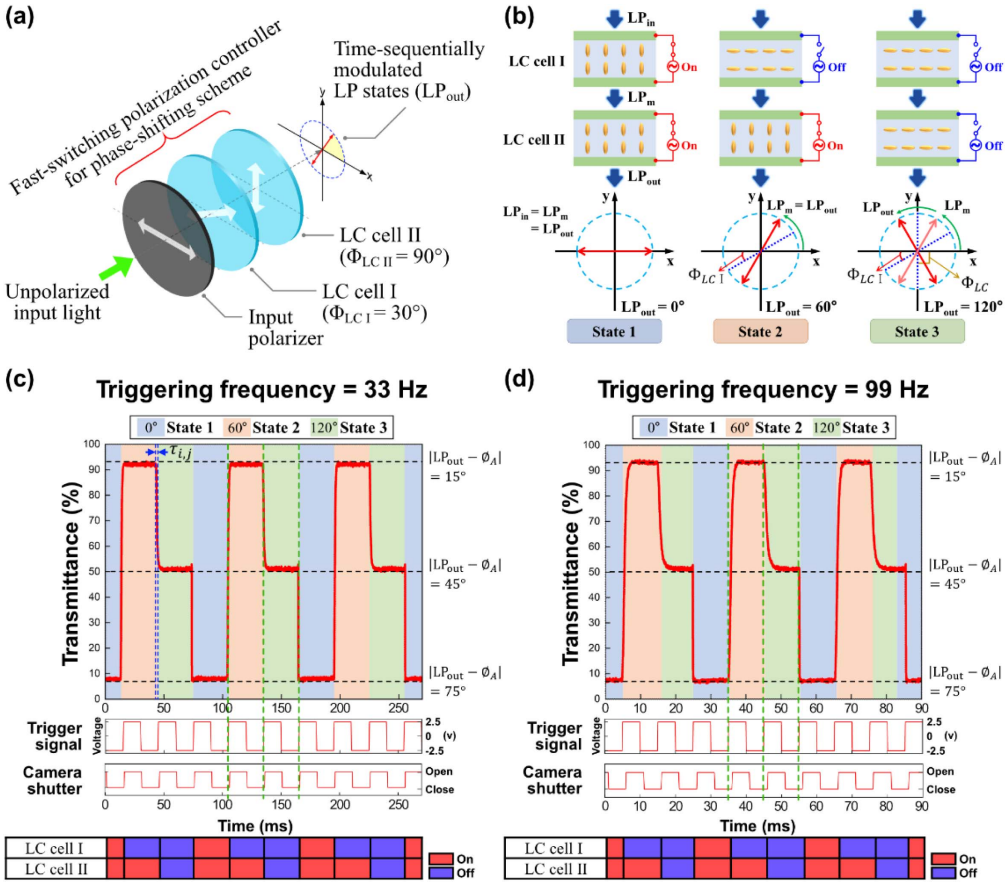

Fig. 2. Fast-switching polarization control unit for temporal polarization-multiplexing scheme with three steps of phase shifting. (a) Bi-stacked LC cells for three-step polarization control. (b) LP_{out} polarization state condition according to LC cell I and LC cell II operation. (c) and (d) Dynamic response characteristics of three-step polarization switching obtained with triggering signal frequency of (c) 33 Hz and (d) 99 Hz, where the LP_{out} state is sequentially switched as 0° → 60° → 120° → 0° and is repeatedly recycled.

in the field-off state, and the polarization angle after light passes through the field-off LC cell can be varied by maintaining the linear polarization state [40,41]. To provide three temporally switching linearly polarized states (LP_{out}) corresponding to 0°, 60°, and 120°, the LC alignment directions of LC cells I and II, denoting the slow axes of the LC cells in the field-off state, are set as $\Phi_{LCI} = 30°$ and $\Phi_{LCII} = 90°$, respectively, with respect to the incident 0° linear polarization (LP_{in}). According to the field-on and field-off combination sets of the bi-stacked LC cells, the intermediate polarization state of LP_m after LC cell I and the final static state of LP_{out} are described in Fig. 2(b). For synchronized operation between the dual-port switching of the bi-stacked LC cells and image capture with camera shutter operation, triggering signals are applied to each unit.

The employed LC cells exhibit a slower field-off switching response than the field-on switching response; this is because the field-on LC dynamics are driven by the field-induced dielectric torque of the LC directors, whereas the field-off LC dynamics are obtained by the cell-thickness-dependent elastic recovery, as discussed in Appendix A [42]. In our bi-stacked LC cells, the switching time ($\tau_{i,j}$) required for the polarization transition between the i state and j state of LP_{out} is dependent on the polarization switching sequence. This is because the switching dynamics of the final LP_{out} are obtained by the combined effect of two different switching dynamics at two LC cells. The temporal switching sequence of LP_{out} is determined for the total $\tau_{i,j}$ for the periodical sweeping of three-state polarization control to be minimized. In our bi-stacked LC cells, the polarization states of LP_{out} are sequentially switched as 0° (state 1) → 60° (state 2) → 120° (state 3) → 0° (repeated state 1). To evaluate the dynamic response characteristics of the bi-stacked LC cells operated for three-step polarization switching, temporal transmittance curves are measured by passing the temporally modulated LP_{out} light through an analyzer (transmission axis: $\Phi_A = 75°$). The switching times $\tau_{i,j}$ for the polarization-state transitions, evaluated with the transmittance dynamics curves shown in Figs. 2(c) and 2(d), obtained by operation at triggering frequencies of 33 Hz and 99 Hz, respectively, are summarized in Table 1.

The total transition time required for one cycle of three-step phase-shifting is sufficiently low (<2.7 ms). Although the three-step phase-shifting scheme is employed for a time-sequential polarization modulation to allow a longer image acquisition time [camera shutter on-time in Figs. 2(c) and 2(d)] at the image sensor, the presented temporally polarization-encoded phase-shifting module is also sufficiently fast for the four-step phase-shifting scheme. For more details on the

Table 1. Switching Time Characteristics of Field-Driven LP_{out} Transition in Three-Step Phase-Shifting Scheme Evaluated under Triggering Frequency Condition Employed for Synchronized LC Cell Operation[a]

LC Switching Condition		Switching Time between LP_{out} Transitions (ms)		
		0° → 60°	60° → 120°	120° → 0°
Triggering frequency for three-step phase-shifting	33 Hz	$\tau_{1,2} = 1.28$	$\tau_{2,3} = 1.18$	$\tau_{3,1} = 0.21$
	99 Hz	$\tau_{1,2} = 1.19$	$\tau_{2,3} = 1.19$	$\tau_{3,1} = 0.20$

[a]$\tau_{i,j}$ denotes the switching time between the i state and j state of LP_{out} polarization modulated by the bi-stacked LC cells.

four-step polarization switching with our bi-stacked LC cells, see Appendix B.

The sequential polarization control of the bi-stacked LC cells operated at triggering frequencies of 33 and 99 Hz corresponds to the holographic video frame rates of 11 and 33 Hz, respectively. For faster polarization switching (< μs), a ferroelectric LC can be employed for the optical axis modulation or retardation control layers instead of the nematic LC used in our experiment [43]. The LP_{out} states controlled by the bi-stacked LC cells are precisely modulated as the desired three steps of the linearly polarized states when the LP_{out} states are evaluated using the transmittance relationship $T = \cos^2(|LP_{out} - \Phi_A|)$, as shown in Figs. 2(c) and 2(d) and Figs. 9(a) and 9(b) (see Appendix B).

3. EXPERIMENTAL SETUP AND RESULT

A. Experimental Setup

The proposed system comprised an objective lens, a bandpass filter, an input linear polarizer, two LC cells, a GP lens, an output linear polarizer, and a nonpolarized high-resolution image sensor. The objective lens collects the illuminating or scattering wavefronts from the object scene. The focal length and diameter of the lens are 100 mm and 1 inch, respectively. Further, the central wavelength of the bandpass filter (#65-159, Edmund Optics) is 550 nm, and the spectral bandwidth is 10 nm. The transmission axis of the input linear polarizer is aligned parallel to the ground surface to initialize the input polarization state to 0°. The LC cells (X-FPM(L)-AR, LC-Tec Displays AB) are connected to the controller (LCC-230, LC-Tec Displays AB) for triggered driving. The clear aperture of the LC cells is 50 mm in diameter. The GP lens (Beam Co.) is followed to modulate the linearly polarized input wavefront into two wavefronts with different radii of curvature, and with orthogonal circular polarization states. The focal length of the GP lens is 240 mm for the 550 nm input light, and the clear aperture is approximately 20 mm in diameter. The distance between the objective lens and the GP lens is about 80 mm. The output polarizer transforms the two orthogonal circularly polarized states into the same polarization state. Interferograms are obtained by a high-resolution and high-frame-rate nonpolarized image sensor (HB-20000SBC, Emergent Vision Technology). The resolution of the image sensor is 4512 × 4512, which corresponds to approximately 20.36 megapixels. The pixel size of the sensor is 2.74 μm in both the horizontal and vertical directions. The image sensor is located about 13 mm behind the GP lens. According to the aforementioned distance relations between the employed optics, the estimated field of view of the employed experimental system is about 35°. Because the proposed method uses the fast temporal phase-shifting method capable of real-time recording, the resultant pixel size for a noise-free complex-valued hologram remains the same as the pixel size of the original interferogram, unlike in the case of parallel phase shifting using a polarized image sensor. The highest frame rate of the image sensor at full resolution is 100 Hz. Because the image sensor has a color filter array for full-color acquisition, only the green channel image is extracted and processed as a hologram after a demosaicking algorithm is applied to the raw image.

A function generator (33500B, Agilent) is used as a triggering source both for the image sensor and LC driver. Two LC cells are operated by the LC driver with the triggering signal from the general-purpose input (GPI) port. The image sensor is also triggered with the opto-isolated GPI port. The exposure of the image sensor starts after a 1 ms delay from the rising pulse of the triggering signal to avoid the transition state of the LC cells and to prevent jittering issues in sequential holographic image acquisitions, which are observed in the timing diagram of Figs. 2(c) and 2(d). The output signal of the function generator and the exposure start and end signals of the image sensor are observed with a connected oscilloscope (MDO34, Tektronix). At first, a stack of raw images is recorded and transferred to the main memory in real time. Then the required per-frame process is followed. The recording process of the raw images is carried out at 99 Hz with the customized software by using the application programming interface provided by the image sensor manufacturer. The elimination of the bias and twin-image noise and the reconstruction process for each frame are performed afterward using MATLAB software. The computation time for each single complex hologram and reconstructed image generation is 1.7 s, with an Intel i9-9920X processor (3.50 GHz) and 64 GB memory, without parallel processing.

B. Validation of Phase-Shifting Performance

To verify the three-step phase-shifting method with the proposed optical configuration, the 200 μm diameter fiber tip coupled with the LED source (MINTF4, Thorlabs) is recorded and reconstructed. Three phase-shifted interferograms are presented in Fig. 3(a). The resolution of each image data is 4512 × 4512 pixels, but presented with a cropped region for better visibility. The bias and twin-image free complex-valued hologram information is shown with the phase-angle data as in Fig. 3(b). In Fig. 3(c), the unwrapped phase profiles of the hologram obtained by the proposed method and by rotating the input polarizer without the LC cells, which are labeled, respectively, as LC and Pol, are compared. The profiles of the unwrapped phase are extracted by following the vertical yellow line indicated in Fig. 3(b). The reconstructed images of LC and

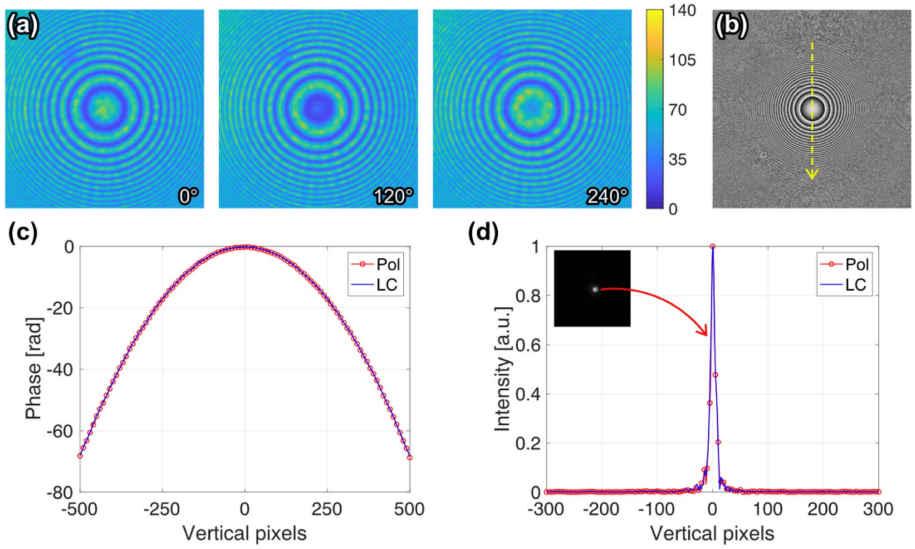

Fig. 3. Recording result of the point-like source. (a) Phase-shifted interferograms. (b) Phase-angle hologram by recombining the images of (a). (c) Unwrapped phase-angle profile of (b), labeled as LC, and the ground truth hologram obtained by the manual stepwise rotation of the input polarizer at 60°, labelled as Pol. (d) Intensity profiles of the images reconstructed from both holograms Pol and LC.

Pol are shown in Fig. 3(d), with the cross-sectional profiles of the intensity values. The reconstruction distance is approximately −158.5 mm in both data.

The unwrapped phase profile validates that the results of the proposed phase-shifting method are almost similar to the results of the phase profile obtained by the manual rotation of the polarizer. The rms error between the two profiles is 0.009. Furthermore, the proposed method is recorded at a speed of 99 Hz without any mechanical movement. The background level around the reconstructed point in Fig. 3(d) is nearly zero, which implies that there is no remaining bias noise. Moreover, no fringe ringing artifact around the point is observed, which might be seen when the defocused twin image remains. Therefore, the elimination performance of twin-image noise of the proposed method is also validated.

C. Demonstration of the Real-Time Holographic Movie with Moving Targets

To demonstrate the fast yet robust phase-shifted hologram acquisition capability of the proposed system, the dynamic scene is recorded with two negative resolution charts in different positions. The experimental setup with two targets is illustrated in Fig. 4(a). The negative 1951 USAF (target 1) and NBS 1963A (target 2) targets are used as sample objects. The distance of each target from the system is about 78 mm and 95 mm, respectively. The targets are presented as two layers with different axial locations by employing the beam combiner, as illustrated in Fig. 4(a). A broadband halogen fiber optic illuminator (OSL2, Thorlabs) is employed as a backlight source. One of the two targets is mounted on the mechanical stage and manually translated in the vertical direction while recording the holograms. The triggering signal for both image sensor exposure and LC state change is set to 99 Hz. Therefore, the resultant frame rate of the hologram and reconstructed movie is 33 Hz. Figures 4(b)–4(d) show the obtained hologram with the phase-angle representation as well as the reconstructed images at different axial positions. The images in Figs. 4(c) and 4(d) are cropped to 1897 × 1897 pixels to present the appearance of the target area clearly, where the cropped region is indicated by the red-dashed box in Fig. 4(b). As a hologram, two targets are focused and blurred, while the reconstruction distance is manipulated accordingly. The dynamic scene of the phase-angle hologram and the reconstructed intensity data are available in Fig. 5 and Visualization 1. Visualization 1 is created by the sequential generation of whole frames of the phase-angle map and the reconstructed image. The reconstruction distance for each frame is indicated in the yellow box in Visualization 1. The distance to focus on each target is configured manually.

The moving dice are recorded as a general object scene with the proposed system. As illustrated in Fig. 6(a), the dice toward the system (Dice 1) is mounted on an optical post and bolted on a motorized rotation stage (PRM1/MZ8, Thorlabs). The dice in the backward direction (Dice 2) is mounted on a flexible gooseneck arm and moved by tapping the arm. The distance of each dice from the system is about 100 mm and 125 mm, respectively, as shown in Fig. 6(a). The dynamic scene is recorded by rotating and moving the dice. While Dice 1 is rotating at 25 deg/s, Dice 2 is tapped by hand to express the dynamic motion. The recorded real-time hologram and reconstructed video are presented in Fig. 7 and Visualization 2, respectively. The resulting movie validates that the proposed method can be effectively used in the real-time incoherent holographic recording system. The static state sample is also presented in Figs. 6(b)–6(d) with the phase-angle hologram and reconstructed images. In these images, 30 frames of the obtained hologram are averaged to enhance the visibility. The reconstructed images are cropped to 1972 × 1972 pixels, where the cropped region is indicated as a red-dashed box in Fig. 6(b). The focus change between the two dice is observed while changing the reconstruction distances from −147 to −155 mm.

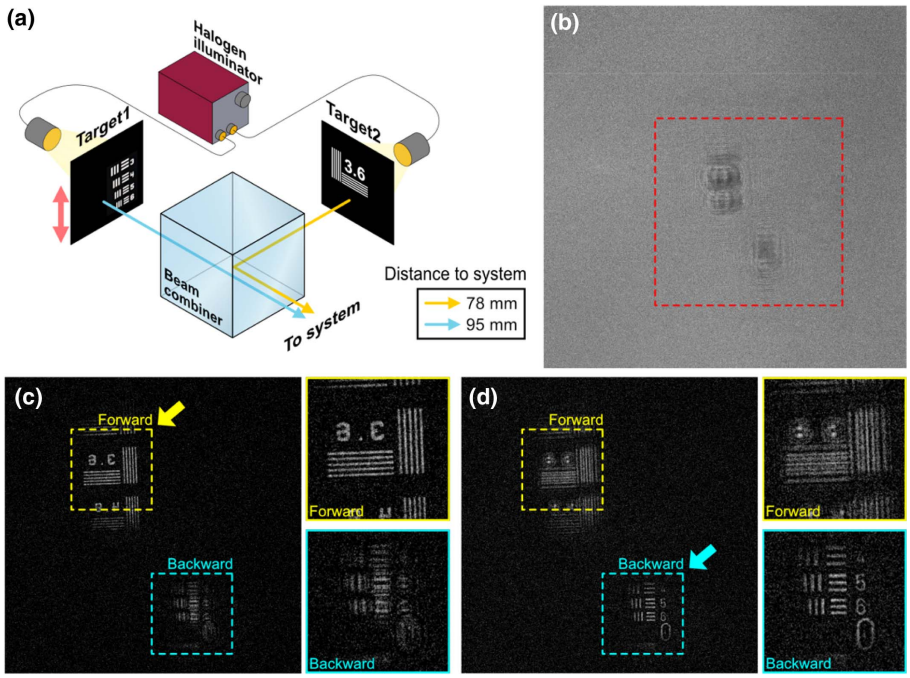

Fig. 4. Experimental result with two negative targets. (a) Target configuration. (b) Phase-angle representation of the obtained hologram. (c) Reconstructed image focused on target 2. (d) Reconstructed image focused on target 1. The reconstructed images are obtained from the region indicated with a dashed-red box in (b).

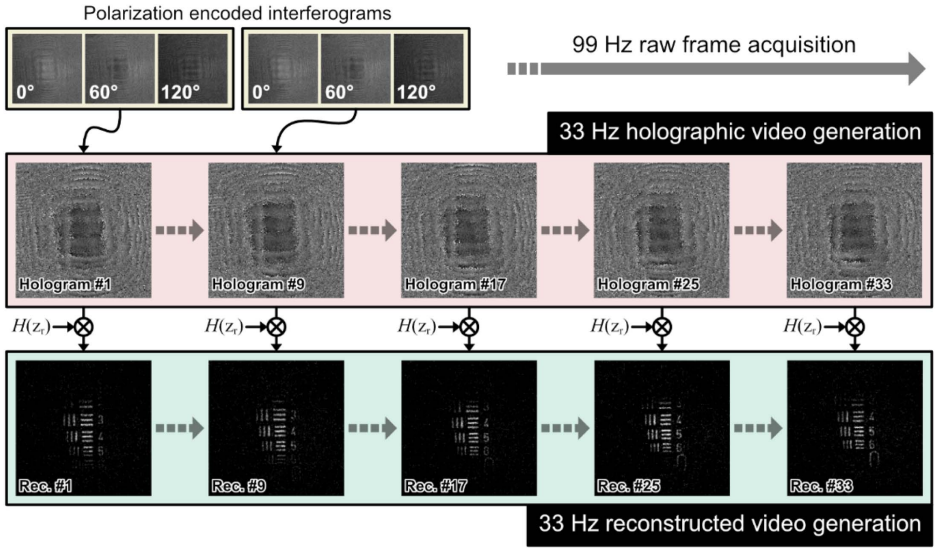

Fig. 5. Illustration of holographic video generation process from raw interferograms to reconstructed image. The holograms are obtained from the targets shown in Fig. 4. The lateral movement of target 1 is observed through frames. The holographic video, including the phase-angle data and reconstructed image at various depth planes, is available in Visualization 1. The convolution kernel $H(z_r)$ and the circle with cross indicate the angular spectrum propagation of the complex hologram field with the distance z_r. Rec., reconstructed image.

4. DISCUSSION AND CONCLUSION

We have demonstrated a real-time self-interference IDH recording system free from bias and twin-image noise by employing the high-speed temporally polarization-encoded phase-shifting method. The three-step phase-shifting is realized by using fast polarization switching LC cells, as well as a high frame rate and a high-resolution nonpolarized image sensor. The IDH video samples are presented with two sample targets: a negative resolution target and two dice. For this demonstration, each phase-shifted interferogram is captured at 99 Hz with a resolution of more than 20 megapixels. The effective frame rate of the processed complex-valued hologram and

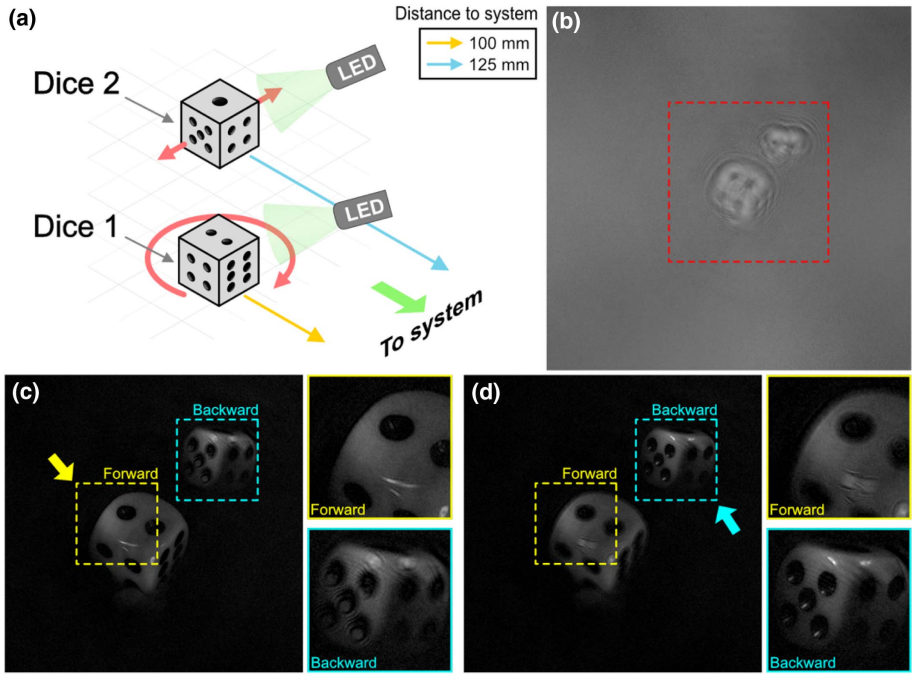

Fig. 6. Hologram of the reflective object. (a) Illustration of the recording scene. (b) Phase-angle map of the obtained hologram. (c) Reconstructed image, focused on the forward object. (d) Reconstructed image, focused on the backward object. 30 holograms are averaged for better visibility. The reconstructed images are cropped, where the region of interest is indicated as a red dashed box in (b).

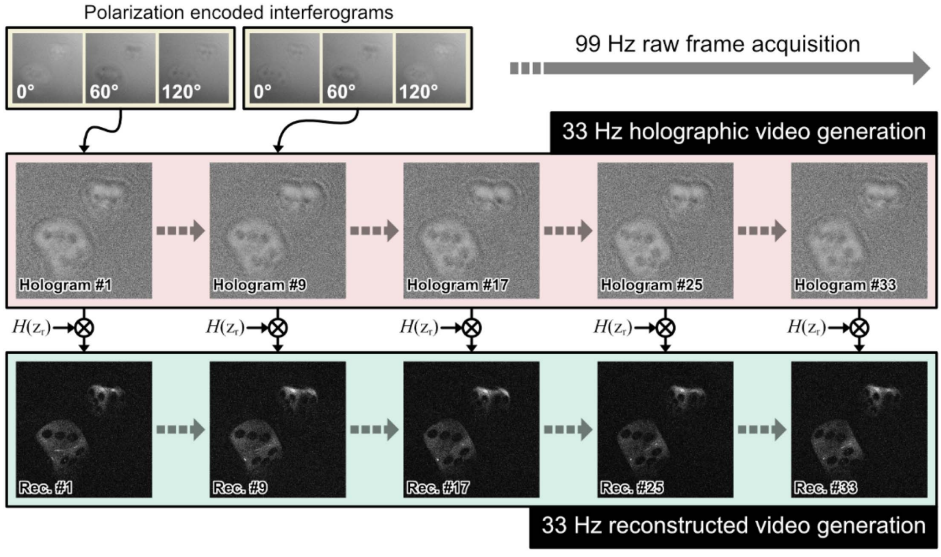

Fig. 7. Illustration of holographic video generation process from raw interferograms to reconstructed image. The holograms are obtained from the targets presented in Fig. 6. The rotation of Dice 1 is observed through frames. The holographic video, including the phase-angle data and reconstructed image at various depth planes, is available in Visualization 2. Rec., reconstructed image.

the reconstructed video is 33 Hz. In this demonstration, the reconstruction of the video hologram is performed after the stack of raw data is acquired in real time. However, if the algorithm is optimized to reconstruct high-resolution holograms in real-time and the computational power is guaranteed, real-time high-resolution holographic streaming could be possible with the proposed method.

In general, parallel phase-shifting technology, which spatially divides and acquires phase-shifted interference fringes using a polarized image sensor, has the advantage of obtaining complex holographic data free from bias and twin image noise with a single exposure, as previously described. However, in this method, four subpixel values with phases shifted by polarizers of different angles are calculated as one complex hologram.

Thus, the number of horizontal and vertical pixels of the obtained complex hologram data is reduced by half. Further, if the resolution of the optical system is sufficiently high and exceeds the Nyquist frequency of the polarized image sensor, the generated holographic fringe pattern might not be faithfully recorded, resulting in the loss of high-fidelity information. The proposed system has the advantage of real-time hologram capture while recording high-frequency fringe patterns faithfully, compared to the system using the polarized image sensor.

From a practical point of view, the polarized image sensor model among various image sensor models on the current market has a limited range of choices. Meanwhile, with the development of the latest wide-bandwidth data transmission technology, numerous image sensors with smaller pixel size and higher resolution while maintaining an acquisition speed close to or higher than 100 Hz are released on the market. Using the proposed method, it is possible to acquire high-quality holograms in real-time using a wide range of state-of-the-art image sensors that do not require additional processes such as lithography for on-chip polarizer fabrication.

As described in Section 2, the amount of the phase shift occurring in the P-GP-P optical structure depends only on the relative angle difference between the two polarizers. In particular, the GP lens, which naturally has a large dependence of the diffraction efficiency on the incident wavelength, reveals an achromatic half-wave retardation upon fabricating the lens with a stack of two chiral LC layers with opposite twist angles [44,45]. As a result, the proposed system should be able to maintain phase-shifting performance uniformly over a wide wavelength range and is supposed to use the entire red, green, and blue pixel aperture of the employed color image sensor to capture full-color holographic information of the object scene. In practice, because the polarization-encoding performance of the LC cells constituting the polarization control unit used in this demonstration is guaranteed only near the designed wavelength, the bandwidth of the incident light is inevitably limited to 10 nm through filtering, and only the green pixel aperture contributes to the hologram image recording. However, the dispersion properties of the polarization control LC module employed for the temporal switching of polarization-encoded phase shifting can be effectively suppressed by adopting achromatic optics designs with additional field-switching LC layers assembled with optically distributed optic axes [46–48]. Thus, the proposed temporal polarization multiplexing scheme is operable while maintaining phase-shifting performance uniformly over a wide wavelength range for the promising full-color IDH system, which will be developed in future studies.

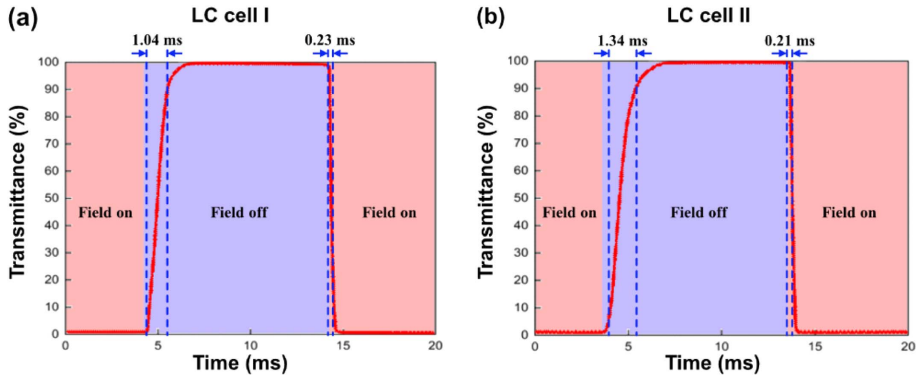

Fig. 8. Switching response of each LC cell: (a) LC cell I and (b) LC cell II.

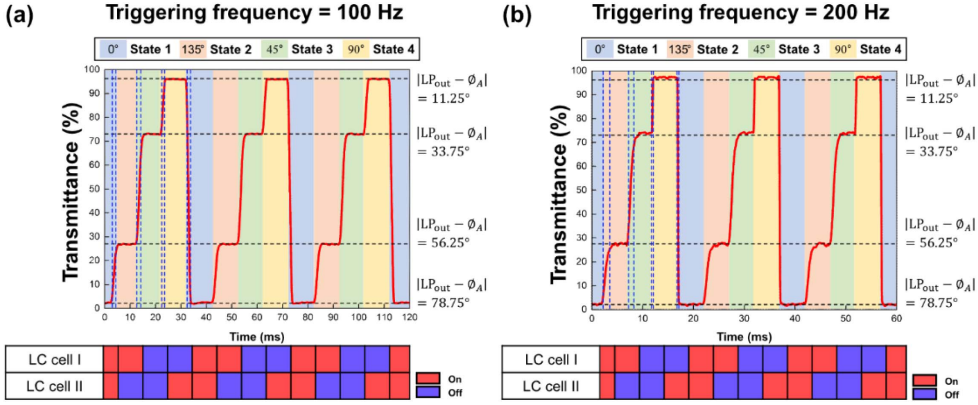

Fig. 9. Dynamic response characteristics of four-step polarization switching, obtained at a triggering signal frequency of (a) 100 Hz and (b) 200 Hz. The switching on and off states for both LC cells for each polarization state (LP_{out}) are plotted.

Table 2. Characteristics of Switching Time between LP_{out} Transitions in Four-Step Phase-Shifting According to the Triggering Frequency Condition

LC Switching Condition		Switching Time between LP_{out} Transitions (ms)			
		0° → 135°	135° → 45°	45° → 90°	90° → 0°
Triggering frequency for four-step phase-shifting	100 Hz	$\tau_{1,2} = 1.14$	$\tau_{2,3} = 1.32$	$\tau_{3,4} = 0.52$	$\tau_{4,1} = 0.50$
	200 Hz	$\tau_{1,2} = 1.22$	$\tau_{2,3} = 1.17$	$\tau_{3,4} = 0.22$	$\tau_{4,1} = 0.20$

APPENDIX A: MEASUREMENT OF SWITCHING RESPONSE OF EACH LC CELL

The dynamic transmittance curves are measured by setting each LC cell between the crossed polarizers, where the optic axis of the LC cell at the field-off state is 45° with respect to the transmission axes of the polarizers. The LC-driving signal used for this evaluation is a square wave, operated at an amplitude of $5V_{pp}$ and frequency of 1 kHz. The results are shown in Fig. 8.

APPENDIX B: MEASURMENT OF CHARACTERISTICS OF FOUR-STEP POLARIZATION SWITCHING WITH BI-STACKED LC CELLS

Figure 2 presents the operation scheme of the three-step polarization switching method with our bi-stacked LC cells and the dynamic response characteristics obtained at a triggering signal frequency of 33 Hz and 99 Hz. Likewise, the high-speed polarization switching from 0° to 135° with a 45° switching interval can be achieved with the proposed method, as shown in Fig. 9 and Table 2. With a two-stacked LC-based polarization control scheme, the polarization states of LP_{out} are sequentially switched as 0° → 135° → 45° → 90° to minimize the switching time delay required between the LP_{out} transitions when the incident polarization state is the linearly polarized $LP_{in} = 0°$. For the four-step phase shifting scheme, the optic axes of the Φ_{LCI} and Φ_{LCII} are set as 45° and 67.5°, respectively. The switching dynamics are characterized by measuring the temporal transmittance variation as a result of LP_{out} changes by passing through an analyzer (transmission axis: $\Phi_A = 78.75°$).

Funding. National Research Foundation of Korea (2019R1A2C1005531); Electronics and Telecommunications Research Institute (23ZH1300); Institute for Information and Communications Technology Promotion (2019-0-00001).

Disclosures. The authors declare no conflicts of interest.

Data Availability. Data underlying the results presented in this paper are not publicly available at this time but may be obtained from the authors upon reasonable request.

REFERENCES

1. J. Rosen and G. Brooker, "Fresnel incoherent correlation holography (finch): a review of research," Adv. Opt. Technol. **1**, 151–169 (2012).
2. J.-P. Liu, T. Tahara, Y. Hayasaki, and T.-C. Poon, "Incoherent digital holography: a review," Appl. Sci. **8**, 143 (2018).
3. J. Rosen, S. Alford, V. Anand, J. Art, P. Bouchal, Z. Bouchal, M.-U. Erdenebat, L. Huang, A. Ishii, S. Juodkazis, N. Kim, P. Kner, T. Koujin, Y. Kozawa, D. Liang, J. Liu, C. Mann, A. Marar, A. Matsuda, T. Nobukawa, T. Nomura, R. Oi, M. Potcoava, T. Tahara, B. L. Thanh, and H. Zhou, "Roadmap on recent progress in FINCH technology," J. Imaging **7**, 197 (2021).
4. J. Rosen and G. Brooker, "Fluorescence incoherent color holography," Opt. Express **15**, 2244–2250 (2007).
5. D. C. Clark and M. K. Kim, "Nonscanning three-dimensional differential holographic fluorescence microscopy," J. Electron. Imaging **24**, 043014 (2015).
6. M. K. Kim, "Full color natural light holographic camera," Opt. Express **21**, 9636–9642 (2013).
7. J. Hong and M. K. Kim, "Single-shot self-interference incoherent digital holography using off-axis configuration," Opt. Lett. **38**, 5196–5199 (2013).
8. X. Quan, O. Matoba, and Y. Awatsuji, "Single-shot incoherent digital holography using a dual-focusing lens with diffraction gratings," Opt. Lett. **42**, 383–386 (2017).
9. C. M. Nguyen, D. Muhammad, and H.-S. Kwon, "Spatially incoherent common-path off-axis color digital holography," Appl. Opt. **57**, 1504–1509 (2018).
10. O. Mudanyali, D. Tseng, C. Oh, S. O. Isikman, I. Sencan, W. Bishara, C. Oztoprak, S. Seo, B. Khademhosseini, and A. Ozcan, "Compact, light-weight and cost-effective microscope based on lensless incoherent holography for telemedicine applications," Lab Chip **10**, 1417–1428 (2010).
11. V. Anand, T. Katkus, D. P. Linklater, E. P. Ivanova, and S. Juodkazis, "Lensless three-dimensional quantitative phase imaging using phase retrieval algorithm," J. Imaging **6**, 99 (2020).
12. Y. Rivenson, Y. Wu, and A. Ozcan, "Deep learning in holography and coherent imaging," Light Sci. Appl. **8**, 85 (2019).
13. T. Zeng, Y. Zhu, and E. Y. Lam, "Deep learning for digital holography: a review," Opt. Express **29**, 40572–40593 (2021).
14. Y.-G. Ju, H.-G. Choo, and J.-H. Park, "Learning-based complex field recovery from digital hologram with various depth objects," Opt. Express **30**, 26149–26168 (2022).
15. G. Pedrini, H. Li, A. Faridian, and W. Osten, "Digital holography of self-luminous objects by using a Mach–Zehnder setup," Opt. Lett. **37**, 713–715 (2012).
16. J. Rosen and G. Brooker, "Digital spatially incoherent Fresnel holography," Opt. Lett. **32**, 912–914 (2007).
17. N. Siegel, V. Lupashin, B. Storrie, and G. Brooker, "High-magnification super-resolution finch microscopy using birefringent crystal lens interferometers," Nat. Photonics **10**, 802–808 (2016).
18. M. V. Berry, "Quantal phase factors accompanying adiabatic changes," Proc. R. Soc. London A **392**, 45–57 (1984).
19. S. Pancharatnam, "Generalized theory of interference, and its applications," Proc. Indian Acad. Sci. A **44**, 247–262 (1956).
20. P. Hariharan and P. Ciddor, "An achromatic phase-shifter operating on the geometric phase," Opt. Commun. **110**, 13–17 (1994).
21. K. Choi, J. Yim, and S.-W. Min, "Achromatic phase shifting self-interference incoherent digital holography using linear polarizer and geometric phase lens," Opt. Express **26**, 16212–16225 (2018).
22. K. Choi, K. Hong, J. Park, and S.-W. Min, "Michelson-interferometric-configuration-based incoherent digital holography with a geometric phase shifter," Appl. Opt. **59**, 1948–1953 (2020).
23. V. Anand, T. Katkus, S. Lundgaard, D. P. Linklater, E. P. Ivanova, S. H. Ng, and S. Juodkazis, "Fresnel incoherent correlation holography with single camera shot," Opto-Electron. Adv. **3**, 200004 (2020).
24. T. Nobukawa, T. Muroi, Y. Katano, N. Kinoshita, and N. Ishii, "Single-shot phase-shifting incoherent digital holography with multiplexed checkerboard phase gratings," Opt. Lett. **43**, 1698–1701 (2018).

25. Y. Zhang, M. T. Wu, M. Y. Tang, F. Y. Ma, E. J. Liang, Y. L. Du, Z. Y. Duan, and Q. X. Gong, "Fresnel incoherent correlation hologram recording in real-time," Optik **241**, 166938 (2021).
26. T. Nobukawa, Y. Katano, M. Goto, T. Muroi, K. Hagiwara, and N. Ishii, "Grating-based in-line geometric-phase-shifting incoherent digital holographic system toward 3D videography," Opt. Express **30**, 27825–27840 (2022).
27. Y. Awatsuji, M. Sasada, and T. Kubota, "Parallel quasi-phase-shifting digital holography," Appl. Phys. Lett. **85**, 1069–1071 (2004).
28. T. Kakue, R. Yonesaka, T. Tahara, Y. Awatsuji, K. Nishio, S. Ura, T. Kubota, and O. Matoba, "High-speed phase imaging by parallel phase-shifting digital holography," Opt. Lett. **36**, 4131–4133 (2011).
29. T. Tahara, T. Kanno, Y. Arai, and T. Ozawa, "Single-shot phase-shifting incoherent digital holography," J. Opt. **19**, 065705 (2017).
30. N. Siegel and G. Brooker, "Single shot holographic super-resolution microscopy," Opt. Express **29**, 15953–15968 (2021).
31. K. Choi, K.-I. Joo, T.-H. Lee, H.-R. Kim, J. Yim, H. Do, and S.-W. Min, "Compact self-interference incoherent digital holographic camera system with real-time operation," Opt. Express **27**, 4818–4833 (2019).
32. D. Liang, Q.-J. Zhang, J. Wang, and J. Liu, "Single-shot Fresnel incoherent digital holography based on geometric phase lens," J. Mod. Opt. **67**, 92–98 (2019).
33. T. Tahara and R. Oi, "Palm-sized single-shot phase-shifting incoherent digital holography system," OSA Contin. **4**, 2372–2380 (2021).
34. Y. Maruyama, T. Terada, T. Yamazaki, Y. Uesaka, M. Nakamura, Y. Matoba, K. Komori, Y. Ohba, S. Arakawa, Y. Hirasawa, Y. Kondo, J. Murayama, K. Akiyama, Y. Oike, S. Sato, and T. Ezaki, "3.2-MP back-illuminated polarization image sensor with four-directional air-gap wire grid and 2.5-μm pixels," IEEE Trans. Electron Devices **65**, 2544–2551 (2018).
35. J. Kim, Y. Li, M. N. Miskiewicz, C. Oh, M. W. Kudenov, and M. J. Escuti, "Fabrication of ideal geometric-phase holograms with arbitrary wavefronts," Optica **2**, 958–964 (2015).
36. L. D. Sio, D. E. Roberts, Z. Liao, S. Nersisyan, O. Uskova, L. Wickboldt, N. Tabiryan, D. M. Steeves, and B. R. Kimball, "Digital polarization holography advancing geometrical phase optics," Opt. Express **24**, 18297–18306 (2016).
37. Y. Takaki, H. Kawai, and H. Ohzu, "Hybrid holographic microscopy free of conjugate and zero-order images," Appl. Opt. **38**, 4990–4996 (1999).
38. T.-C. Poon and J.-P. Liu, *Introduction to Modern Digital Holography: With MATLAB* (Cambridge University, 2014).
39. S. Kumar, *Liquid Crystals: Experimental Study of Physical Properties and Phase Transitions* (Cambridge University, 2000).
40. J. E. Bigelow and R. A. Kashnow, "Poincaré sphere analysis of liquid crystal optics," Appl. Opt. **16**, 2090–2096 (1977).
41. G. R. Fowles, *Introduction to Modern Optics* (Courier Corporation, 1989).
42. D.-K. Yang and S.-T. Wu, *Fundamentals of Liquid Crystal Devices* (Wiley, 2014).
43. H.-R. Kim, Y. W. Lee, S.-J. Kim, D.-W. Kim, C.-J. Yu, B. Lee, and S.-D. Lee, "A rotatable waveplate using a vertically aligned deformed-helix ferroelectric liquid crystal," Ferroelectrics **312**, 57–62 (2004).
44. C. Oh and M. J. Escuti, "Achromatic diffraction from polarization gratings with high efficiency," Opt. Lett. **33**, 2287–2289 (2008).
45. N. V. Tabiryan, S. V. Serak, S. R. Nersisyan, D. E. Roberts, B. Y. Zeldovich, D. M. Steeves, and B. R. Kimball, "Broadband waveplate lenses," Opt. Express **24**, 7091–7102 (2016).
46. M. D. Lavrentovich, T. A. Sergan, and J. R. Kelly, "Switchable broadband achromatic half-wave plate with nematic liquid crystals," Opt. Lett. **29**, 1411–1413 (2004).
47. J. L. Vilas, L. M. Sanchez-Brea, and E. Bernabeu, "Optimal achromatic wave retarders using two birefringent wave plates," Appl. Opt. **52**, 1892–1896 (2013).
48. L. Li and M. J. Escuti, "Super achromatic wide-angle quarter-wave plates using multi-twist retarders," Opt. Express **29**, 7464–7478 (2021).